Topology optimized gold nanostrips for enhanced near-infrared photon upconversion

Vester-Petersen, Joakim; Christiansen, Rasmus Ellebæk; Julsgaard, Brian; Balling, Peter; Sigmund, Ole; Madsen, Søren Peder

Published in:
Applied Physics Letters

Link to article, DOI:
10.1063/1.4998552

Publication date:
2017

Document Version
Publisher's PDF, also known as Version of record

Topology optimized gold nanostrips for enhanced near-infrared photon upconversion

Joakim Vester-Petersen, Rasmus E. Christiansen, Brian Julsgaard, Peter Balling, Ole Sigmund, and Søren P. Madsen

Citation: Appl. Phys. Lett. **111**, 133102 (2017); doi: 10.1063/1.4998552
View online: http://dx.doi.org/10.1063/1.4998552
View Table of Contents: http://aip.scitation.org/toc/apl/111/13
Published by the American Institute of Physics

Topology optimized gold nanostrips for enhanced near-infrared photon upconversion

Joakim Vester-Petersen,[1,a)] Rasmus E. Christiansen,[2] Brian Julsgaard,[3,4] Peter Balling,[3,4] Ole Sigmund,[2] and Søren P. Madsen[1]
[1]*Department of Engineering, Aarhus University, Inge Lehmanns Gade 10, 8000 Aarhus C, Denmark*
[2]*Department of Mechanical Engineering, Technical University of Denmark, Nils Koppels Alle, Building 404, 2800 Kgs. Lyngby, Denmark*
[3]*Department of Physics and Astronomy, Aarhus University, Ny Munkegade 120, 8000 Aarhus C, Denmark*
[4]*Interdisciplinary Nanoscience Center (iNANO), Aarhus University, Gustav Wieds Vej 14, 8000 Aarhus C, Denmark*

(Received 1 August 2017; accepted 8 September 2017; published online 25 September 2017; publisher error corrected 29 September 2017)

This letter presents a topology optimization study of metal nanostructures optimized for electric-field enhancement in the infrared spectrum. Coupling of such nanostructures with suitable ions allows for an increased photon-upconversion yield, with one application being an increased solar-cell efficiency by exploiting the long-wavelength part of the solar spectrum. In this work, topology optimization is used to design a periodic array of two-dimensional gold nanostrips for electric-field enhancements in a thin film doped with upconverting erbium ions. The infrared absorption band of erbium is utilized by simultaneously optimizing for two polarizations, up to three wavelengths, and three incident angles. Geometric robustness towards manufacturing variations is implemented considering three different design realizations simultaneously in the optimization. The polarization-averaged field enhancement for each design is evaluated over an 80 nm wavelength range and a ±15-degree incident angle span. The highest polarization-averaged field enhancement is 42.2 varying by maximally 2% under ±5 nm near-uniform design perturbations at three different wavelengths (1480 nm, 1520 nm, and 1560 nm). The proposed method is generally applicable to many optical systems and is therefore not limited to enhancing photon upconversion. *Published by AIP Publishing.* [http://dx.doi.org/10.1063/1.4998552]

The optical properties of metal nanostructures receive attention due to their ability to generate highly localized electromagnetic fields allowing for technological advancements. Applications include nanoscale resolution for near-field optical microscopy,[1] optically assisted data storage,[2] chemical sensing on a single molecular level,[3] and enhanced ionic luminescence.[4,5] This work focuses on the latter, with one application being single-junction solar cells, which suffer from considerable transmission losses as sub-band-gap photons do not provide enough energy for the electron-hole generation. Depending on the material as well as the technology used, these transmission losses account for a significant fraction of the incident solar power: 59% for organic (P3HT:PCBM)[6] and 19% for crystalline silicon (c-Si)[6] solar cells. The losses can, however, be reduced by upconverting sub-band-gap photons into photons with energy larger than the band-gap energy, and thereby increase the overall efficiency, potentially beyond the Shockley-Queisser limit.[7] Upconversion in erbium ions, Er^{3+}, by photon absorption at wavelengths, λ, between $1400\,\text{nm} \leq \lambda \leq 1600\,\text{nm}$[6,8,9] and subsequent photon emission at $\lambda = 980\,\text{nm}$ is appropriate for the 1.1 eV band-gap energy of c-Si corresponding to $\lambda \simeq 1100\,\text{nm}$. Theoretical studies[10] have shown a power-law dependence, relating the intensity of the upconverted light, I_{UC}, to the intensity of the incident light, I_{in}, as $I_{UC} \propto I_{in}^{m}$ with m experimentally found to be ≈ 1.5 at $\lambda = 1500\,\text{nm}$.[5] The upconverted light intensity is assumed related to the incident electric field norm as $I_{UC} \propto I_{in} \propto \|\boldsymbol{E}\|^{2m} \simeq \|\boldsymbol{E}\|^{3}$. Under the natural solar irradiance, upconversion in Er^{3+} is negligible due to a low light intensity and a small absorption cross section of Er^{3+}. To overcome this, enhancement of the light intensity incident on Er^{3+} using metal nanostructures has been proposed and demonstrated to show increased upconversion.[4,11,12] The field enhancement depends in a complex fashion on the nanostructure composition and geometry, the surrounding environment, as well as the wavelength, polarization, and propagation direction of the excitation field.

Plasmonically enhanced upconversion has been measured experimentally using nanoparticles of silver (Ag), excited at $\lambda = 808\,\text{nm}$,[4] and gold (Au) excited at $\lambda = 980\,\text{nm}$ (Ref. 12) and $\lambda = 1500\,\text{nm}$.[5] In these studies, the nanoparticle shape, size, and arrangement were numerically tuned using parameter-based optimization, aiming at enhancement of the incident light under monochromatic excitation at normal incidence. These choices are likely to severely limit the potential upconversion yield, partly due to a low utilization at other excitation wavelengths within the ion absorption band and partly due to low field amplification at oblique angles. Furthermore, none of the nanoparticles were optimized for robustness against manufacturing variations which can lead to performance discrepancies when physically realizing numerical designs.[4]

The aim of this work is to increase the photon upconversion yield by exploiting the full infrared absorption band of Er^{3+} at multiple angles of incidence using geometrically

a)jvepe@eng.au.dk

robust, field-enhancing metal nanostructures. To achieve this goal, topology optimization is used to create 2D cross-sectional designs of embedded Au nanostrips (infinitely long in the out-of-plane direction), capable of enhancing the incident light within an Er^{3+} doped thin film. A complete upconverter-assembly placed at the rear of a solar cell could upconvert infrared photons and reflect them back towards the solar cell using a mirror.

Topology optimization[13] is a computational tool originally developed for mechanical design problems.[14] However, the method is very versatile and has been applied to a wide range of areas such as micro-electro-mechanical systems,[15] acoustics,[16–18] nano-photonics,[19] and plasmonics.[20–22] Topology optimization works by varying the spatial distribution of different materials within a bounded design domain. The design problem is formulated as an optimization problem with the goal of finding the material distribution minimizing or maximizing an objective function, measuring the quantity to be optimized. The design is described by a pixel or voxel representation in which a design variable is associated with each mesh element. Consequently, no explicit design parameterization is needed, and the design is changed without geometrical constraints such as those imposed when using parameter-based shape or size optimization.

In topology optimization, the (numerical) density approach[14,23] relaxes the discrete nature of placing different materials within individual mesh elements by introducing a set of element-wise constant design variables, ρ_e, allowed to take any continuous value between 0 and 1. Subsequent filtering[24] and projection[25] steps are applied to ρ_e, obtaining the physical element-wise density distribution, $\bar{\tilde{\rho}}_e = \bar{\tilde{\rho}}_e(\boldsymbol{\rho})$, where $\boldsymbol{\rho}$ is a vector containing all design variables. During the optimization process, the physical densities are forced towards 0 or 1 using a smooth threshold-projection scheme[17,25] Topology optimization is able to handle large-scale optimization problems with more than 100 million design variables[26] leaving almost unlimited freedom in the design process. Topology optimization is a gradient based method and relies on adjoint sensitivity analysis,[19,27] for efficient calculation of design sensitivities. For more details of the topology optimization framework, the reader is referred to the references stated above and references therein.

The 2D model problem considered in this work is shown in Fig. 1. The model consists of a top domain of air, $\boldsymbol{\Omega}_{\text{Top}}$,

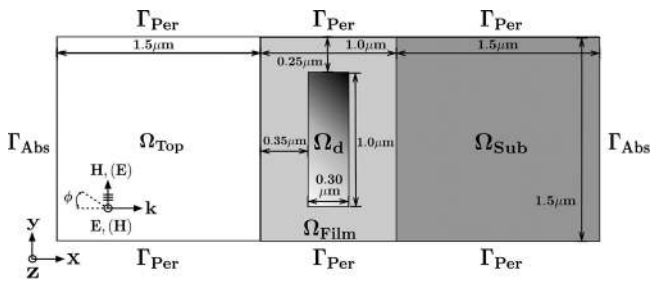

FIG. 1. Unit cell of the 2D model setup. Top domain, $\boldsymbol{\Omega}_{\text{Top}}$, design domain, $\boldsymbol{\Omega}_{\text{d}}$, film domain, $\boldsymbol{\Omega}_{\text{Film}}$, and substrate domain, $\boldsymbol{\Omega}_{\text{Sub}}$. The computational domain is truncated by imposing Floquet-Bloch periodicity[28] at $\boldsymbol{\Gamma}_{\text{Per}}$, and absorbing boundary conditions[29] at $\boldsymbol{\Gamma}_{\text{Abs}}$. Directions of the exciting fields are shown for E_z (H_z) polarization. The wave propagation of the excitation field is in the positive x-direction with incident angle, ϕ.

and an Er^{3+} doped TiO_2 (TiO_2:Er) film, $\boldsymbol{\Omega}_{\text{Film}}$, deposited on a SiO_2 substrate, $\boldsymbol{\Omega}_{\text{Sub}}$. I_{UC} is changed by distribution of either Au or TiO_2:Er within the design domain, $\boldsymbol{\Omega}_{\text{d}}$, that is embedded into the film ($\boldsymbol{\Omega}_{\text{d}} \subset \boldsymbol{\Omega}_{\text{Film}}$). The model is excited by an E_z- or H_z-polarized plane wave propagating in the positive x-direction with incident angle ϕ. Assuming translational symmetry in the z-direction and linear polarization of $\boldsymbol{E}$ and $\boldsymbol{H}$, the total electric field is obtained by solving the scalar Helmholtz equation[30] using the finite element method.[30] All materials are assumed non-magnetic, and the relative magnetic permeability is set to $\mu_r(\boldsymbol{r}) = 1$. The complex relative electric permittivity, $\hat{\epsilon}_r$, is calculated using the refractive index, η, and extinction coefficient, κ, as $\hat{\epsilon}_r = \epsilon_r' + i\epsilon_r'' = \eta^2 - \kappa^2 + i2\eta\kappa$. The material properties for Au and SiO_2 are taken from Johnson[31] and Malitson,[32] respectively, while values for TiO_2:Er were experimentally obtained using ellipsometry to be $(\eta,\ \kappa) \approx (2.26,\ 0.00)$ for all considered λ. The material properties inside $\boldsymbol{\Omega}_{\text{d}}$ are linearly interpolated in $\eta(\bar{\tilde{\rho}}_e)$ and $\kappa(\bar{\tilde{\rho}}_e)$ between TiO_2:Er and Au, with $\bar{\tilde{\rho}}_e = 0$ corresponding to TiO_2:Er and $\bar{\tilde{\rho}}_e = 1$ corresponding to Au.

The objective function is chosen as

$$\Phi_{ijk} = \frac{1}{2}\sum_{E_z,H_z} \frac{\int_{\boldsymbol{\Omega}_{\text{Film}}} (1 - H(\bar{\tilde{\boldsymbol{\rho}}_i}))\|\boldsymbol{E}(\bar{\tilde{\boldsymbol{\rho}}_i}, \lambda_j, \phi_k)\|^3 d\boldsymbol{\Omega}}{\int_{\boldsymbol{\Omega}_{\text{Film}}} \|\boldsymbol{E}(\boldsymbol{0}, \lambda_j, \phi_k)\|^3 d\boldsymbol{\Omega}}, \quad (1)$$

due to the desire of enhancing $I_{\text{UC}} \propto \|\boldsymbol{E}\|^3$. The sum is over the two polarizations, $\bar{\tilde{\boldsymbol{\rho}}}$ is a vector containing all physical densities, λ is the excitation wavelength, and ϕ is the angle of incidence. Φ_{ijk} is normalized with respect to the background field, $\boldsymbol{E}(\boldsymbol{0}, \lambda, \phi)$, and is thus a direct measure of the I_{UC} enhancement relative to a situation without Au present in the design domain. Φ_{ijk} is evaluated in the entire film domain[4,5] in order to provide a measure for the upconversion yield enhancement over the entire domain.

$H(\bar{\tilde{\boldsymbol{\rho}}})$ is a smoothed Heaviside function with $H(\bar{\tilde{\boldsymbol{\rho}}} = 0) = 0$ and $H(\bar{\tilde{\boldsymbol{\rho}}} > 0) \approx 1$. As no Er^{3+} ions are present in the Au any internal electric fields are excluded from affecting the value of Φ_{ijk}, using the factor $(1 - H(\bar{\tilde{\boldsymbol{\rho}}}))$ in the numerator. Quenching[33] is not taken into account in this work, however it can potentially be included in Φ_{ijk} by reformulation of $H(\bar{\tilde{\boldsymbol{\rho}}})$.

A ± 5 nm robustness, towards near-uniform geometric design variations such as those associated with production inaccuracies, is included using the double-filter approach,[17] which is an extension to the original robust approach.[34] Geometrical robustness is taken into account by considering three design realizations $\boldsymbol{\rho}_i$, $i \in \{1, 2, 3\}$ where the nominal design ($\boldsymbol{\rho}_2$), is eroded ($\boldsymbol{\rho}_1$) and dilated ($\boldsymbol{\rho}_3$) by 5 nm, respectively. The numbering of $\boldsymbol{\rho}_i$ is in order of increased structure size. While the chosen robustness and design complexity challenge standard lithography processes, emerging production techniques such as helium ion deposition[35] or other future advances could enable the physical realization of the proposed designs.

Φ_{ijk} is optimized for incident wavelengths λ_j, and angles of incidence ϕ_k. The optimization problem is formulated as a *min max* problem, minimizing the worst performing design realization in the set $\{-\Phi_{ijk}\}$, and the nominal design is therefore not guaranteed to obtain the highest objective function value.

Table I shows the parameters considered for the four optimization cases, A–D, together with a reference case, R. The reference case is a rectangle of solid Au centered in $\mathbf{\Omega}_\mathrm{d}$ with dimensions tuned to maximize Φ using a parameter scan of the width, $W \in [10\,\mathrm{nm},\ 1000\,\mathrm{nm}]$, and height, $H \in [10\,\mathrm{nm},\ 300\,\mathrm{nm}]$, resulting in $(W,\ H) = (600\,\mathrm{nm},\ 150\,\mathrm{nm})$. The interval for λ is sampled at 3 equally spaced wavelengths with the central wavelength $\lambda = 1520\,\mathrm{nm}$ used for the two single-wavelength cases A and B. Normal incidence is chosen for cases optimized for one angle of incidence only (A and C). Three incident angles are chosen for cases B and D, $\phi = \{0°,\ 7.5°,\ 15°\}$. In order to reduce the required computational time, 3 wavelengths and 3 incident angles are considered, although a larger amount could easily be included. All optimizations are started from the same initial design with all design variables set to 0.5, corresponding to a mix between TiO_2:Er and Au. Reflection symmetry of $\boldsymbol{\rho}$ is applied along the x-axis at the center of $\mathbf{\Omega}_\mathrm{d}$ corresponding to $\phi = \{-15°,\ -7.5°,\ 0,\ 7.5°,\ 15°\}$.

A MATLAB implementation is used to solve the discretized model problem using the finite element method and the optimization is performed using the Globally Convergent Method of Moving Asymptotes (GCMMA).[36,37] All plots are shown for the nominal design $\boldsymbol{\rho}_2$. All designs are performance validated in COMSOL Multiphysics®[38] with regions near dielectric-metal interfaces discretized using 1 nm linear elements to resolve skin effects and other artifacts associated with dielectric-plasmonic interfaces.

The polarization-averaged field enhancement within $\mathbf{\Omega}_\mathrm{Film}$ is shown in Fig. 2 for all five cases at $(\lambda,\ \phi) = (1520\,\mathrm{nm},\ 0°)$ and $(\lambda,\ \phi) = (1560\,\mathrm{nm},\ 15°)$. The field enhancements for cases R and A are significantly reduced at non-optimized wavelengths and incident angles, while all multi-parameter cases (B-D) are seen to maintain a more consistent performance for the two situations illustrated in Fig. 2. It is also observed that different features on the nano-strips interact with the field when varying λ and ϕ. The contours of the optimized designs are highlighted by the light blue line with the line thickness representing the imposed geometric robustness of $\pm 5\,\mathrm{nm}$. The summed objective value for each design realization together with the performance relative to the nominal design is shown in Table II. Cases A and R are directly comparable, as they are optimized at the same λ and ϕ. Here, the nominal topology optimized design outperforms the reference by approximately a factor of 3 with $\sum_{jk} \Phi_{2jk} = 179.9$ and $\sum_{jk} \Phi_{2jk} = 54.7$, respectively. Comparing instead to an optimized circle leads to the same conclusion result, but with a larger factor in favor of the topology optimized design.

TABLE I. Considered wavelengths, λ, angles of incidence, ϕ, for the reference case, R, and optimized cases, A-D.

Case	λ [nm]	ϕ[°]
R	1520	0
A	1520	0
B	1520	0, 7.5, 15
C	1480, 1520, 1560	0
D	1480, 1520, 1560	0, 7.5, 15

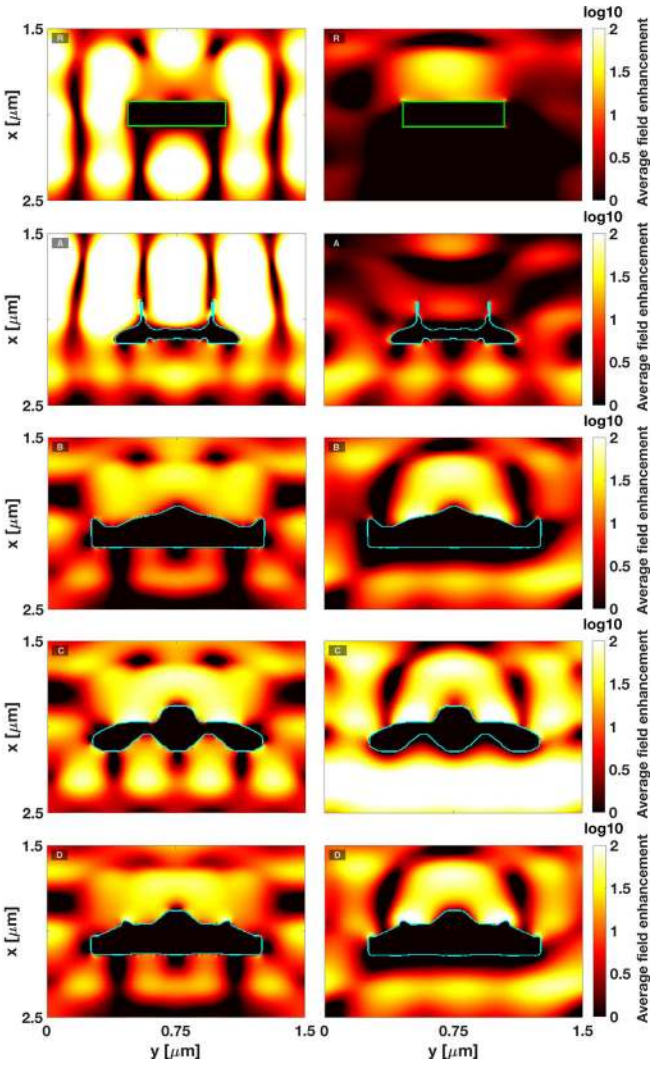

FIG. 2. Polarization-averaged field enhancement in the film domain, $\mathbf{\Omega}_\mathrm{Film}$: $log_{10}\frac{1}{2}\sum_{E_z,H_z} \|\boldsymbol{E}\|^3 / \|\boldsymbol{E}_0\|^3$ for cases R, A-D. Left column: $(\lambda,\ \phi) = (1520\ \mathrm{nm},\ 0°)$. Right column: $(\lambda,\ \phi) = (1560\ \mathrm{nm},\ 15°)$. The design robustness is shown in blue with the line thickness representing the difference between the dilated and eroded design. For case R, this is shown in green with the eroded and dilated design created manually. Here, the wave propagation is in the positive x-direction (top to bottom).

The design robustness is, however, directly comparable across all five cases. Here, all topology optimized designs show decreased sensitivity towards geometric perturbations compared to the reference. Case C performs almost

TABLE II. Summed objective values for each design realization together with the design robustness; $\frac{\sum \Phi_{1jk}}{\sum \Phi_{2jk}}$ and $\frac{\sum \Phi_{3jk}}{\sum \Phi_{2jk}}$ denoting the performance of the eroded and dilated designs relative to the nominal design, respectively. Sums are over λ_j and ϕ_k; $\sum_{jk}$. Direct comparison, across cases, is only possible between the highlighted numbers of the same color.

Case	Eroded $\sum \Phi_{1jk}$	Nominal $\sum \Phi_{2jk}$	Dilated $\sum \Phi_{3jk}$	Robustness $\frac{\sum \Phi_{1jk}}{\sum \Phi_{2jk}}$	Robustness $\frac{\sum \Phi_{3jk}}{\sum \Phi_{2jk}}$
R	16.7	54.7	27.2	0.30	0.50
A	225.1	179.9	112.9	1.25	0.63
B	31.1	38.3	50.4	0.81	1.32
C	56.7	55.7	54.8	1.02	0.99
D	130.1	123.9	120.7	1.05	0.97

identically across all realizations, having a maximum performance variation of 2%, a significant reduction compared to case R with a maximum performance decrease of 70%. Additionally, the performance sensitivity was tested when changing the film thickness (x-dir.) and width (y-dir.) by ± 20 nm relative to the dimensions shown in Fig. 1. Both cases R and A showed a high performance decline while all cases optimized for multiple λ and/or multiple ϕ (B-D) proved less sensitive with near consistent performance.

The main objective of this work is to obtain designs with high field enhancements and with low sensitivity towards changes in wavelength and incident angle. This is investigated by mapping the performance of the nominal design $\Phi_{2lm} = \Phi(\boldsymbol{\rho}_2, \lambda_l, \phi_m)$ of all cases across a wide wavelength and angle span; $\lambda_l \in [1400\,\text{nm}, 1600\,\text{nm}]$ and $\phi_m \in [0°, 87.5°]$, which allows for a direct performance comparison of all cases. The map of Φ_{2lm} is shown in Fig. 3 for cases R, A, and C. Case A clearly outperforms the reference at $(\lambda, \phi) = (1520\,\text{nm}, 0°)$ and case C obtains high overall field enhancements. The average design performance, $\langle \Phi_2 \rangle_{lm}$, is evaluated in the interval spanned by the minimum and maximum λ_j and ϕ_k considered in case D, and is shown in Table III. All topology optimized designs offer a higher average performance compared to the reference design, with case C having the highest average of $\langle \Phi_2 \rangle_{lm} = 42.2$, corresponding to a normalized average performance gain of $\langle \Phi_2 \rangle^{\star}_{lm} = 4.8$ relative to the reference case R.

Figure 3 shows that each design has multiple local peaks with extremely high values of Φ_{2lm} which affects $\langle \Phi_2 \rangle^{\star}_{lm}$ and could potentially result in a misleading average performance

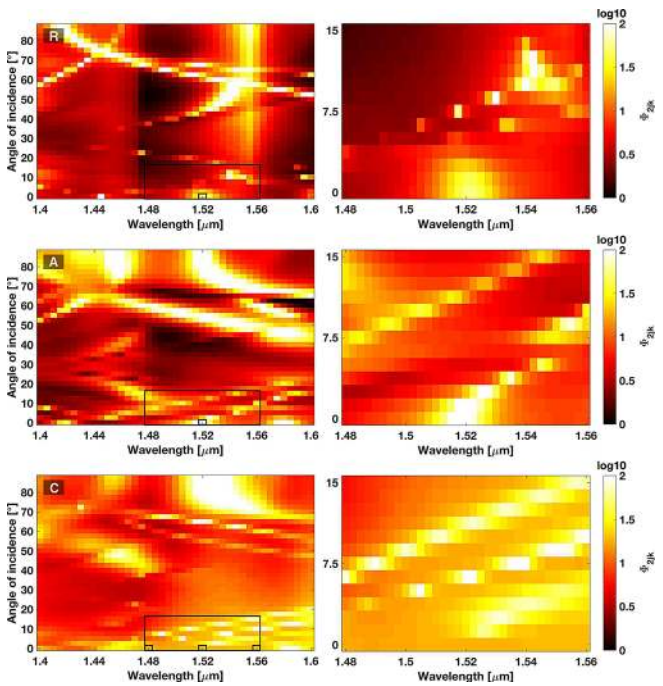

FIG. 3. Objective value for the nominal design, Φ_{2lm}, for cases R, A and C. Left column: $\lambda_l \in [1400\,\text{nm}, 1600\,\text{nm}]$ and $\phi_m \in [0°, 87.5°]$ with increments $(\Delta\lambda_l, \Delta\phi_m) = (5\,\text{nm}, 2.5°)$. Black squares indicate the discrete values of λ and ϕ considered in the optimization. $\langle \Phi_2 \rangle_{lm}$ is evaluated in the black rectangular box. Right column: zoom-in of the black rectangle, $\lambda_l \in [1480\,\text{nm}, 1660\,\text{nm}]$ and $\phi_m \in [0°, 15°]$ with increments $(\Delta\lambda_l, \Delta\phi_m) = (2.5\,\text{nm}, 1.25°)$. Due to design symmetry, the mapped performance is symmetric around $\phi = 0°$; here, only positive values of ϕ are shown.

TABLE III. Objective function values averaged across the λ-range by ϕ-span enclosed by the rectangular box shown in Fig. 3. The averages, normalized with respect to case R, are denoted $\langle \Phi_2 \rangle^{\star}_{lm}$ and normalized averages truncated to a maximum enhancement of 1000 and 100 are given by $\langle \Phi_2 \rangle^{\star 1000}_{lm}$ and $\langle \Phi_2 \rangle^{\star 100}_{lm}$, respectively. Absolute averages are shown in parentheses for convenience.

Case	$\langle \Phi_2 \rangle^{\star}_{lm}$	$\langle \Phi_2 \rangle^{\star 1000}_{lm}$	$\langle \Phi_2 \rangle^{\star 100}_{lm}$
R	1.0 (8.7)	1.0 (8.7)	1.0 (8.3)
A	1.7 (14.4)	1.7 (14.4)	1.6 (13.4)
B	3.6 (31.4)	3.2 (27.9)	2.4 (20.3)
C	4.8 (42.2)	3.8 (33.3)	3.2 (26.4)
D	3.8 (33.0)	3.1 (27.4)	2.4 (19.8)

indication. In order to limit the influence of these localized peaks, values of Φ_{2lm} in the rectangular box in Fig. 3 are truncated to a maximum of 1000 and 100 and the average performance is shown in Table III as $\langle \Phi_2 \rangle^{\star 1000}_{lm}$ and $\langle \Phi_2 \rangle^{\star 100}_{lm}$, respectively. The size of the box spans the interval between the minimum and maximum wavelength and incident angle considered in the optimization (see Table I).

Despite truncation, the highest average performance is still obtained using the design from case C with $\langle \Phi_2 \rangle^{\star 1000}_{lm} = 3.8$ and $\langle \Phi_2 \rangle^{\star 100}_{lm} = 3.2$. These results indicate that a design optimized for multiple wavelengths (case C) implicitly possesses decreased sensitivity towards angular variations. This is possibly due to the larger change of the wavevector component in the propagation direction when changing λ_j compared to changing ϕ_k. Decreased sensitivity has also been reported in acoustic design problems[17] using multi-frequency optimization. Including both several wavelengths and several incident angles (case D) did not result in an increased performance. The many requirements here may have over constrained the problem and caused convergence to a local optimum. Restarting the optimization with other starting guesses may potentially lead to better designs.

Consequently, the conjecture that optimizing for multiple wavelengths may implicitly cause a design to be more robust against angular variations can be utilized to save computational resources and hinder convergence to local minima when performing a full 3D optimization; a task which, is computationally orders of magnitude more expensive.

This work clearly demonstrates the strength of topology optimization as a design tool for optimizing field enhancing metallic nanostructures. The topology optimized designs are geometrically non-intuitive and maintain their high-performance over a large wavelength and angular-spectrum. The best-performing gold nanostrip achieve a polarization-averaged field amplification of $\Phi > 42$ compared to having no nanostrip embedded in the TiO_2:Er thin film and significantly exceeds the performance offered by a simple rectangular reference design by a factor of 4.8. In addition, the sensitivity to manufacturing variations decreased from 70% to 2% partly by optimizing for multiple wavelengths and partly by including geometric design perturbations of ± 5 nm in the optimization process, leaving the design robust towards production inaccuracies.

Although the resulting optimized structures are not overly complex, they will still present a challenge for realization using standard lithography processes. Nevertheless,

this study demonstrates the potential gain in going to more complex geometries and thus provides motivation for further improvement of manufacturing methods.

The developed framework is by no means restricted to optimization of $\|\boldsymbol{E}\|^3$ for enhancing upconversion. Reformulating the objective function (e.g., by weighting λ_j and ϕ_k and/or including quenching effects), boundary conditions, materials, etc., allows the method to be easily adapted to multitude of interesting optimization problems in nano-optics.

The authors thank the *Innovation Fund Denmark* for funding this research under the project *SunTune* (4106-00002B) and Ph.D. Fellow, Harish Lakhotiya from the Department of Physics and Astronomy at Aarhus University, for ellipsometry measurements of the TiO_2:Er.

[1]H. G. Frey, F. Keilmann, A. Kriele, and R. Guckenberger, Appl. Phys. Lett. **81**, 5030 (2002).
[2]M. Mansuripur, A. R. Zakharian, A. Lesuffleur, S.-H. H. Oh, R. J. Jones, N. C. Lindquist, H. Im, A. Kobyakov, and J. V. Moloney, Opt. Express **17**, 14001 (2009).
[3]G. Logan Liu, IEEE J. Sel. Top. Quantum Electron. **16**, 662 (2010).
[4]S. R. Johannsen, S. P. Madsen, B. R. Jeppesen, J. V. Nygaard, B. Julsgaard, P. Balling, and A. N. Larsen, Appl. Phys. Lett. **106**, 053101 (2015).
[5]H. Lakhotiya, A. Nazir, S. P. Madsen, J. Christiansen, E. Eriksen, J. Vester-Petersen, S. R. Johannsen, B. R. Jeppesen, P. Balling, A. N. Larsen, and B. Julsgaard, Appl. Phys. Lett. **109**, 263102 (2016).
[6]J. C. Goldschmidt and S. Fischer, Adv. Opt. Mater. **3**, 510 (2015).
[7]W. Shockley and H. J. Queisser, J. Appl. Phys. **32**, 510 (1961).
[8]C. Strohhöfer and A. Polman, Opt. Mater. **21**, 705 (2003).
[9]S. Fischer, B. Fröhlich, H. Steinkemper, K. Krämer, and J. Goldschmidt, Sol. Energy Mater. Sol. Cells **122**, 197 (2014).
[10]M. Pollnau, D. R. Gamelin, S. R. Lüthi, H. U. Güdel, and M. P. Hehlen, Phys. Rev. B **61**, 3337 (2000).
[11]H. Mertens and A. Polman, Appl. Phys. Lett. **89**, 211107 (2006).
[12]H. P. Paudel, D. Dachhepati, K. Bayat, S. S. Mottaghian, P. S. May, C. Lin, S. Smith, and M. F. Baroughi, J. Photonics Energy **3**, 035598 (2013).
[13]M. P. Bendsøe and O. Sigmund, *Topology Optimization* (Springer, 2004).
[14]M. P. Bendsøe and N. Kikuchi, Comput. Methods Appl. Mech. Eng. **71**, 197 (1988).
[15]O. Sigmund, Comput. Methods Appl. Mech. Eng. **190**, 6577 (2001).
[16]M. B. Dühring, J. S. Jensen, and O. Sigmund, J. Sound Vib. **317**, 557 (2008).
[17]R. E. Christiansen, B. S. Lazarov, J. S. Jensen, and O. Sigmund, Struct. Multidiscip. Optim. **52**, 737 (2015).
[18]R. E. Christiansen and O. Sigmund, Appl. Phys. Lett. **109**(10), 101905 (2016).
[19]J. S. Jensen and O. Sigmund, Laser Photonics Rev. **5**, 308 (2011).
[20]J. Andkjær, S. Nishiwaki, T. Nomura, and O. Sigmund, J. Opt. Soc. Am. B **27**, 1828 (2010).
[21]M. B. Dühring, N. Asger Mortensen, and O. Sigmund, Appl. Phys. Lett. **100**, 211914 (2012).
[22]Y. Deng, Z. Liu, C. Song, P. Hao, Y. Wu, Y. Liu, and J. G. Korvink, Struct. Multidiscip. Optim. **53**, 967 (2016).
[23]M. P. Bendsøe, Struct. Optim. **1**, 193 (1989).
[24]J. K. Guest, J. H. Prévost, and T. Belytschko, Int. J. Numer. Methods Eng. **61**, 238 (2004).
[25]F. Wang, B. S. Lazarov, and O. Sigmund, Struct. Multidiscip. Optim. **43**, 767 (2011).
[26]N. Aage, E. Andreassen, and B. S. Lazarov, Struct. Multidiscip. Optim. **51**, 565 (2015).
[27]D. A. Tortorelli and P. Michaleris, Inverse Probl. Sci. Eng. **1**, 71 (1994).
[28]J.-M. Jin, *Theory and Computation of Electromagnetic Fields* (John Wiley & Sons, Inc., 2010).
[29]K. Dossou, M. A. Byrne, and L. C. Botten, J. Comput. Phys. **219**, 120 (2006).
[30]J.-M. Jin, *The Finite Element Method in Electromagnetics*, 3rd ed. (Wiley-IEEE Press, 2014).
[31]P. B. Johnson and R. W. Christy, Phys. Rev. B **6**, 4370 (1972).
[32]I. H. Malitson, J. Opt. Soc. Am. **55**, 1205 (1965).
[33]S. Fischer, D. Kumar, F. Hallermann, G. von Plessen, and J. C. Goldschmidt, Opt. Express **24**, A460 (2016).
[34]O. Sigmund, Acta Mech.Sin./Lixue Xuebao **25**, 227 (2009).
[35]S. A. Boden, Z. Moktadir, D. M. Bagnall, H. Mizuta, and H. N. Rutt, Microelectron. Eng. **88**, 2452 (2011).
[36]K. Svanberg, Int. J. Numer. Methods Eng. **24**, 359 (1987).
[37]K. Svanberg, SIAM J. Optim. **12**, 555 (2002).
[38]COMSOL AB, "COMSOL Multiphycis™ v. 5.2a".